Article

Synthesis of Nanostructured Mg₂Ni for Hydrogen Storage by Mechanical Alloying via High-Pressure Torsion

Edgar Ignacio López Gómez [1,2,*], Joaquín Gonzalez [2], Jorge M. Cubero-Sesin [2] and Jacques Huot [1,*]

[1] Hydrogen Research Institute, Université du Québec à Trois-Rivières, 3351 Boul. des Forges, Trois-Rivières, Québec, QC G9A 5H7, Canada

[2] Centro de Investigación y Extensión en Materiales (CIEMTEC), Escuela de Ciencia e Ingeniería de los Materiales, Instituto Tecnológico de Costa Rica (ITCR), Cartago 159-7050, Costa Rica; jegonzalez@tec.ac.cr (J.G.); jcubero@itcr.ac.cr (J.M.C.-S.)

[*] Correspondence: edgar.ignacio.lopez.gomez@uqtr.ca (E.I.L.G.); jacques.huot@uqtr.ca (J.H.)

Abstract: Mg₂Ni is a highly promising candidate for solid-state hydrogen storage due to its high storage capacity. However, its synthesis is challenging due to the high melting point of Ni (1455 °C) and the boiling point of Mg (1090 °C). In this study, elemental powder mixtures of Mg and 30 at% Ni were processed by high-pressure torsion (HPT) to synthesize the Mg₂Ni intermetallic compound through mechanical methods. The formation of 11 wt% of Mg₂Ni after 50 turns of HPT was confirmed by X-ray diffraction (XRD), scanning electron microscopy (SEM), and energy-dispersive spectroscopy (EDS), reaching a maximum of 59 wt% after 100 turns. Rietveld refinement confirmed a nanocrystalline size for the Mg₂Ni phase synthesized via HPT. Hydrogenation tests showed that the Mg-Ni synthesized by HPT can absorb hydrogen at 350 °C even after several weeks of air exposure. Furthermore, a maximum absorption capacity of 3.8 wt% was reached after 20 h of hydrogen exposure for the sample with 100 turns. This capacity is close to the theoretical capacity of 3.9 wt% for this composition. The results confirm that combining HPT with subsequent heat treatment is an efficient strategy to increase the Mg₂Ni fraction after HPT processing.

Keywords: severe plastic deformation (SPD); hydrogen storage; metal hydrides; magnesium–nickel intermetallics; nanostructured alloys

1. Introduction

It is widely recognized that hydrogen serves as an excellent clean energy carrier and has the potential to be utilized in both stationary and mobile applications [1–3]. Hydrogen possesses a gravimetric energy density over three times higher than common hydrocarbon fuels [3]. Nevertheless, various technical aspects of hydrogen storage materials and systems constrain industrial applications. Nowadays, methods involving gas or cryogenic liquid states are commonly utilized for hydrogen storage [1–3]. For instance, hydrogen-powered vehicles utilize high-pressure gas stored at 70 MPa [2,4]. However, the high cost and volume of these tanks limit their application in fields with higher energy demands [1–3].

Solid-state systems using metal hydrides is another safe means of hydrogen storage. Theoretically, pure Mg can absorb 7.6 wt% H, pure Al can absorb 11 wt% H, and alloys such as LaNi₅ and TiFe can absorb 1.5 wt% and 1.8 wt% H, respectively. However, the thermodynamic properties of metal hydrides are one of the main factors that prevent the adoption of solid-state systems [5–13]. Mg is one of the most promising elements due to its relatively high storage capacity and low weight. Unfortunately, a high desorption temperature makes its implementation as a hydrogen storage material difficult. Therefore, the development of new materials that will store hydrogen in a solid state is vital for the widespread application of hydrogen as a clean energy carrier at the industrial level.

Different methods have been applied to modify the hydrogen storage properties of metal hydrides. Chemical modification by alloying, i.e., Mg-Ni and Ti-Fe alloys, cata-

lysts such Zr and oxides (Nb_2O_5, Fe_3O_4, V_2O_5, TiO_2) [14–22], solid solutions (Ti-Cr-Fe, TiFe-O) [14,23], and other methods have demonstrated positive effects in modifying the hydrogenation properties of pure metals [11,24]. In the Mg-Ni system, the Mg_2Ni intermetallic phase shows good properties for solid-state hydrogen storage, with a theoretical gravimetrical capacity of 3.8 wt% H.

However, the synthesis process of Mg_2Ni and Mg-Ni alloys is a complicated procedure using common metallurgical methods, mainly due to the low boiling point of Mg (1090 °C) and the high melting point of Ni (1455 °C). In addition, the phase diagram Mg-Ni involves a peritectic and a eutectic reaction taking place subsequently during the cooling process [25]; therefore, products such as $MgNi_2$ are also produced, reducing the yield and the hydrogen storage capacity.

To limit this temperature gap, different researchers have shown the effectiveness of mechanical alloying processes such ball milling [26–33] and cold rolling [34,35], with good results in the synthesis of Mg_2Ni and other compounds. Emami et al. processed powder mixtures of Mg-33 at% X by HPT, with X corresponding to 21 different elements including Ni [36]. Emami et al. reported the synthesis of $Mg_{17}Al_{12}$, MgZn, MgAg, Mg_2In, and Mg_2Sn under a pressure of 3 GPa for 100 turns. They reported a phase transformation to Mg_2Ni just after an HT post-HPT. Additionally, the intermetallic compound TiFe has previously been synthesized after 10 turns [37]. Other immiscible systems such as Mg-Zr [38], Mg-Ti [39], and Mg-Hf [40] has also previously been synthesized by HPT.

Severe plastic deformation (SPD) methods, such as HPT [41–43] and equal-channel angular processing (ECAP) [44–48], have been used due to their capacity to achieve high strain and grain refinement even in metals with high hardness. SPD has also been shown to produce fast hydrogen transport on casted intermetallics due to the high density of grain boundaries and crystalline defects, also enhancing the activation and hydrogenation kinetics [36,49–59].

Mechanical processing has also shown good results in the thermal activation of TiFe and in the kinetics of absorption via the effect of grain refinement [11]. In Mg alloys, the effect of grain refinement shows improvements in the kinetics of absorption [11,26,28,32,60]. Hongo et al. reported the formation of nanograins and stacking faults in Mg_2Ni ingots processed by HPT, with a high hydrogen capacity (3.3 wt% H at 150 °C) and improved absorption kinetics with respect to the annealed ingot material [58]. Edalati et al. also synthesized homogeneous Mg_4NiPd alloy with a bcc structure and low hydrogen binding energy by using the HPT process for 1500 turns. This alloy reversibly absorbed and desorbed 0.7 wt% H at 32 °C [59]. However, previous HPT studies do not show any evidence of the synthesis of Mg_2Ni from the binary powder mixture as in ball milling [26–33] and cold rolling [34].

In this work, we systematically studied the synthesis of nanocrystalline Mg_2Ni using the HPT process under higher pressures of up to 6 GPa, starting from a binary elemental powder mixture close to the stoichiometric composition. The main advantages of the HPT method in contrast to the ball milling technique are the absence of an inert atmosphere [34], the reduction in contamination during the process [61,62], and the absence of a reactive powder after milling. The microstructure, crystal structure, and hydrogen storage properties of materials were investigated.

2. Materials and Methods

2.1. Materials

High-purity Mg powder (99.8%) from Thermo Scientific Chemicals (Waltham, MA USA), with a particle size below 250 μm, was mixed with 30 at% of high-purity Ni (99.99%) from Millipore Sigma Canada Ltd (Oakville, ON, Canada), with a particle size below 150 μm. The powders were mixed by manual stirring for 3 min and by ultrasonic bathing in acetone for 7 min; this was repeated for 30 min. Then, the acetone was evaporated completely. The powder mixture was pre-compacted into a disc shape of 10 mm diameter in a manual hydraulic press.

2.2. HPT Procedure and Equipment

The pre-compacted discs were processed by HPT under 6 GPa of pressure at ambient temperature for 3, 10, 20, 40, 50, 88, and 100 turns (now referred to as N3, N10, N20, N50, N40, N88, and N100 samples, respectively) with a rotation speed of 1 rpm. The powders and the samples were processed and manipulated in an air atmosphere. The γ induced in HPT can be considered as the shear strain described in Equation (1), where r is the distance from the center of the disc, N is the number of turns during the HPT, and h is the thickness of the disc [63].

$$\gamma = \frac{2\pi r N}{h} \tag{1}$$

A custom HPT equipment consisting of a four-column hydraulic press with a capacity of 200 tons (YH32-200 XZPRESTEK) and a electromechanical torsion machine (SISELEC SA, San José, Costa Rica) was used. The discs were placed between two anvils of D2 tool steel in the torsion system, each with a cavity of 10 mm diameter and 0.5 mm depth for the sample processing.

2.3. Characterization Methods

The samples were examined by XRD using a Bruker Focus D8 diffractometer with Cu Kα radiation. Rietveld analysis using TOPAS [64,65] was carried out to quantify the phase composition. The samples were also examined by SEM using a Hitachi SU1510 instrument equipped with an Oxford Instruments X-Max EDS to evaluate the microstructural evolution and the chemical composition. The hydrogen storage performance was measured using a homemade Sieverts apparatus at 350 °C under a hydrogen pressure of 2000 kPa.

3. Results and Discussion

3.1. Synthesis and Characterization of Mg$_2$Ni by HPT

The phase formation and the microstructural evolution in the Mg-Ni mixtures after HPT were examined by XRD at different numbers of turns. The XRD pattern given in Figure 1 shows the results taken near the edge of the discs for the samples with 10, 50, and 100 turns. After 10 turns, slight variations can be observed in the diffraction pattern of Mg and Ni phases in comparison to the powder mixture. Peak broadening was observed in the Ni phase, which gave a crystallite size reduction to 82 nm, while Mg showed mainly only changes in the intensities of diffracting planes, with a crystallite size of 163 nm. Table 1 summarizes the phase composition and lattice parameters of the powder mixture, and the HPT samples processed by 10, 50, and 100 turns. According to the XRD results in Table 1, Mg and Ni do not show a large change in their crystal size from 10 to 50 turns. Further processing after 100 turns shows a crystallite size reduction in Mg and Ni to 70 μm and 57 μm, respectively.

The XRD pattern given in Figure 1 clearly shows new broad peaks appearing after 100 turns, which are centered at ~19.8° and ~39.8°, suggesting the growth of a new nanocrystalline phase. According to the XRD analysis and Rietveld refinement results, it was possible to identify that these peaks fit well to the Bragg peaks of Mg$_2$Ni with hcp structure P6$_2$22. After 100 turns, 59 wt% of the Mg$_2$Ni phase was identified, with a crystallite size of 6 nm. Furthermore, even after 50 turns, it was possible to identify 11 wt% of the Mg$_2$Ni phase.

The formation of the Mg$_2$Ni phase was also analyzed by XRD in different regions of the HPT disc processed for 100 turns. In addition to the edge scan, the disc sample was scanned at the center, both at the upper and lower surfaces (where γ is lower, theoretically in a region corresponding to strains from 0 to 3100), according to Equation (1). Figure 2 shows the XRD pattern results of Mg-30 at% Ni processed for 100 turns in the aforementioned disc regions and corresponding strain levels, while Table 2 shows the phase composition and lattice parameters of the resulting phases.
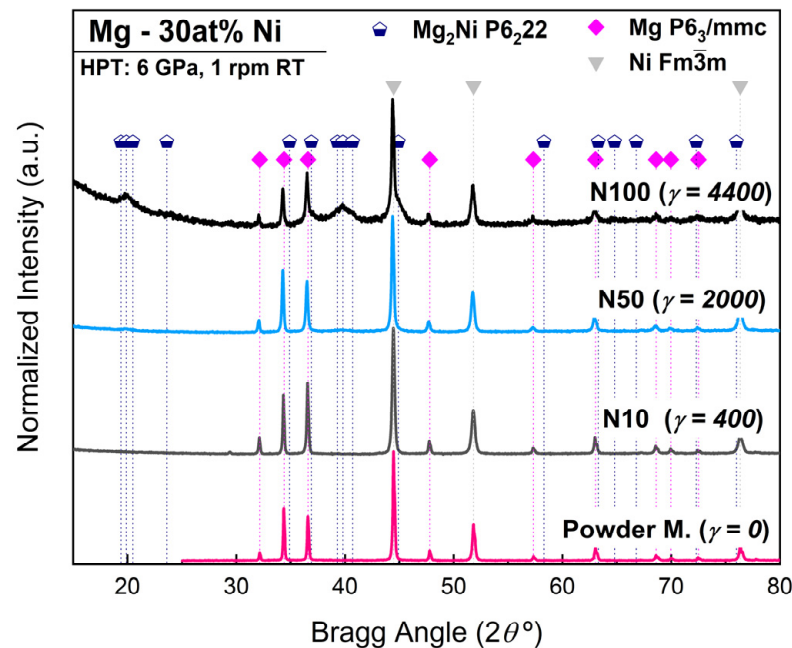
Figure 1. XRD patterns of Mg-Ni initial powder mixture and after HPT processing for 10, 50, and 100 turns showing gradual formation of nanostructured Mg_2Ni by HPT.

Table 1. Crystallographic parameters of phases present in Mg-30 at% Ni powder mixture and processed by 10, 50, and 100 turns of HPT.

Condition	Phase	wt%	a (Å)	c (Å)	Crystallite Size (nm)
Powder Mixture	Mg hcp	46 (3)	3.2102 (3)	5.2118 (1)	-
	Ni fcc	54 (5)	3.5251 (2)	-	-
HPT N10 $\gamma = 400$	Mg hcp	44 (3)	3.2104 (1)	5.2125 (2)	163 (7)
	Ni fcc	56 (3)	3.5252 (1)	-	82 (2)
HPT N50 $\gamma = 2000$	Mg hcp	42 (2)	3.2101 (2)	5.2110 (3)	168 (2)
	Ni fcc	47 (3)	3.5246 (1)	-	80 (2)
	Mg_2Ni hcp	11 (2)	5.27 (1)	13.35 (6)	6 (1)
HPT N100 $\gamma = 4400$	Mg hcp	18 (2)	3.2099 (4)	5.2129 (6)	70 (3)
	Ni fcc	24 (3)	3.5249 (3)	-	57 (1)
	Mg_2Ni hcp	59 (3)	5.230 (2)	13.30 (1)	6 (1)

The XRD patterns in Figure 2 and Rietveld refinement results in Table 2 show that the Mg_2Ni phase clearly increased from the upper (21 wt%) to the lower surface (30 wt%). Such differences across the thickness of the disc could happen as result of slippage between the sample and anvils, especially at a high number of turns [66]. Also, in comparison with the results in Table 1, Mg_2Ni reaches a maximum of 59 wt% at the edge of the disc after HPT processing, where the strain reaches the maximum in the radial direction ($\gamma = 4400$). Also, for the Mg and Ni phases, the crystallite size decreases at the edge of the sample where the shear strain is highest. Rietveld refinement confirms a crystallite size of less than 6 nm for the Mg_2Ni hcp phase, which is in good agreement with previous HPT processes, where Mg-Ti [39], Mg-Zr [38], and Mg-based immiscible systems were also synthesized [41,58,59,67].
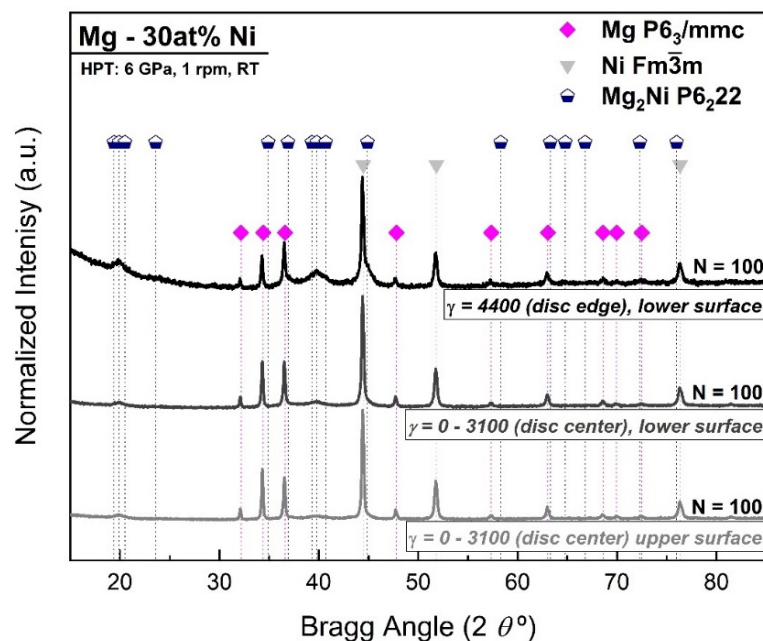
Figure 2. XRD patterns of Mg-30 at% Ni at upper surface ($\gamma = 0$ by theory), lower surface ($\gamma = 3100$), and edge of the disc ($\gamma = 4400$) showing the formation of nanostructured Mg_2Ni when the strain by HPT increases.

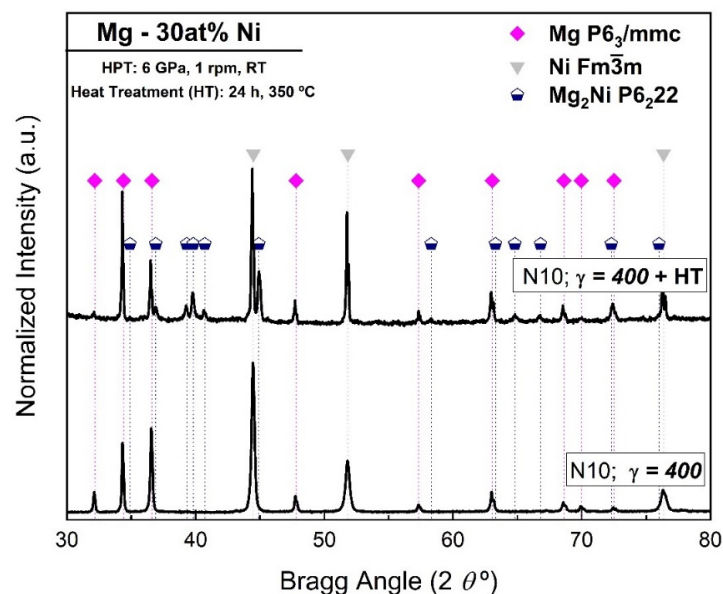**Table 2.** Crystallographic parameters of phases present in Mg-30 at% Ni processed by HPT for 100 turns.

Condition	Phase	wt%	a (Å)	c (Å)	Crystallite Size (nm)
HPT N100	Mg hcp	34 (2)	3.2124 (2)	5.2148 (3)	156 (11)
$\gamma = 0$–3100	Ni fcc	44 (3)	3.5267 (1)	-	89 (2)
Upper surface	Mg_2Ni hcp	21 (2)	5.252 (5)	13.35 (3)	6 (3)
HPT N100	Mg hcp	31 (2)	3.2108 (2)	5.2119 (3)	121 (7)
$\gamma = 0$–3100	Ni fcc	39 (2)	3.5258 (2)	-	76 (6)
Lower surface	Mg_2Ni hcp	30 (2)	5.248 (6)	13.39 (3)	5 (2)

The effect of an HT was also studied for the Mg-30 at% Ni processed by 10 turns of HPT. Figure 3 shows the results for Mg-30 at% Ni after 10 turns, with (N10, $\gamma = 400$ + HT) and without HT (N10, $\gamma = 400$). In Figure 3, it is possible to observe that after the HT, the peaks belonging to Mg_2Ni can clearly be seen and correspond to 34 wt%, as shown in Table 3.

These results confirm that even when the Mg_2Ni phase was not observed in the sample after 10 turns, the HT post-HPT enhanced the formation of the Mg_2Ni phase. This is consistent with the work of Emami et al. [36]. The results also show grain growth in the Ni and Mg phases after the HT. The Ni phase crystallite size increased from 82 nm to 146 nm, while the Mg phase increased from 163 nm to a size too large to be accurately measured by XRD. The Rietveld results also show that after the HT, the crystallite size of the Mg_2Ni phase remains at a nano size (85 nm) and Ni remains at an ultra-fine size (146 nm). Regarding the XRD analysis in Figures 1–3 and Tables 1–3, there is no evidence of oxide formation after the HPT process or after the HT, at least under the detection limit of the XRD technique.

Figure 3. XRD patterns of Mg-30 at% Ni processed by HPT for 10 turns (γ = 400) with and without heat treatment.

Table 3. Crystallographic parameters of phases present in Mg-30 at% Ni processed by HPT for 10 turns (γ = 400) after heat treatment at 350 °C for 24 h.

Condition	Phase	wt%	a (Å)	c (Å)	Crystallite Size (nm)
HPT N10	Mg hcp	33 (2)	3.2110 (2)	5.2106 (2)	-
γ = 400	Ni fcc	33 2)	3.5251 (1)	-	146 (7)
HT 350 °C	Mg$_2$Ni hcp	34 (2)	5.2196 (3)	13.2713 (18)	85 (5)

SEM-EDS was performed at different distances from the center of the disc, to analyze at the micrometer level the elemental distribution of Mg and Ni and the degree of mixing. Figure 4 shows the results for Mg-30 at% Ni processed after 5 (Figure 4a–c), 40 (Figure 4d–g), and 100 (Figure 4h–k) turns. After five turns (Figure 4a–c), the images reveal that Mg and Ni are completely separated from each other, showing dark and bright contrast regions, respectively. The EDS elemental mapping shown in Figure 4a,c confirms this statement. Further HPT processing shows an improvement in the Mg-Ni intermixing, as can be seen in Figure 4d–k. Also, when increasing the number of turns (i.e., from 5 to 40 turns) and increasing the distance from the center of the disc (up to 5 mm), the particle size of Mg and Ni is reduced, improving the mixing of the elements. This behavior is in good agreement with previous reports, where the homogeneity of the elemental powder mixture increases with the increase in the strain for Mg-Al [68], Mg-Zr [38], Al-Fe [69], Cu-Ta [70], Nb-Ti [71], and Ti-Nb [72]. The samples also show a clear torsional shear deformation pattern at the center of the disc after 5 and 40 turns (Figure 4a,d), which becomes less evident after 100 turns (Figure 4h). In general, after 100 turns, a randomly oriented microstructure was developed due to the increment of the homogeneity and the phase transformation to Mg$_2$Ni. Figure 4 confirms that there are some spots at the edge of the disc where the complete mixture occurred, showing a single-phase contrast. The EDS elemental mapping analysis in Figure 5 shows a composition ratio of Mg to Ni of ~2 at the edge of the sample (62.2 at% Mg to 29.9 at% Ni). It was also possible to observe that some surface oxides (7.9 at%) were formed after the HPT process, which are mainly over the Mg phase. In addition, the average of spectra 10, 11, 12, and 13 shown in Figure 5 are 63 at% ($\pm$4), 28 at% ($\pm$6), and 7 at% ($\pm$1) of Mg, Ni, and O, respectively. Thus, the experimental composition identified by EDS is consistent with the Mg$_2$Ni phase identified by XRD and Rietveld refinement.
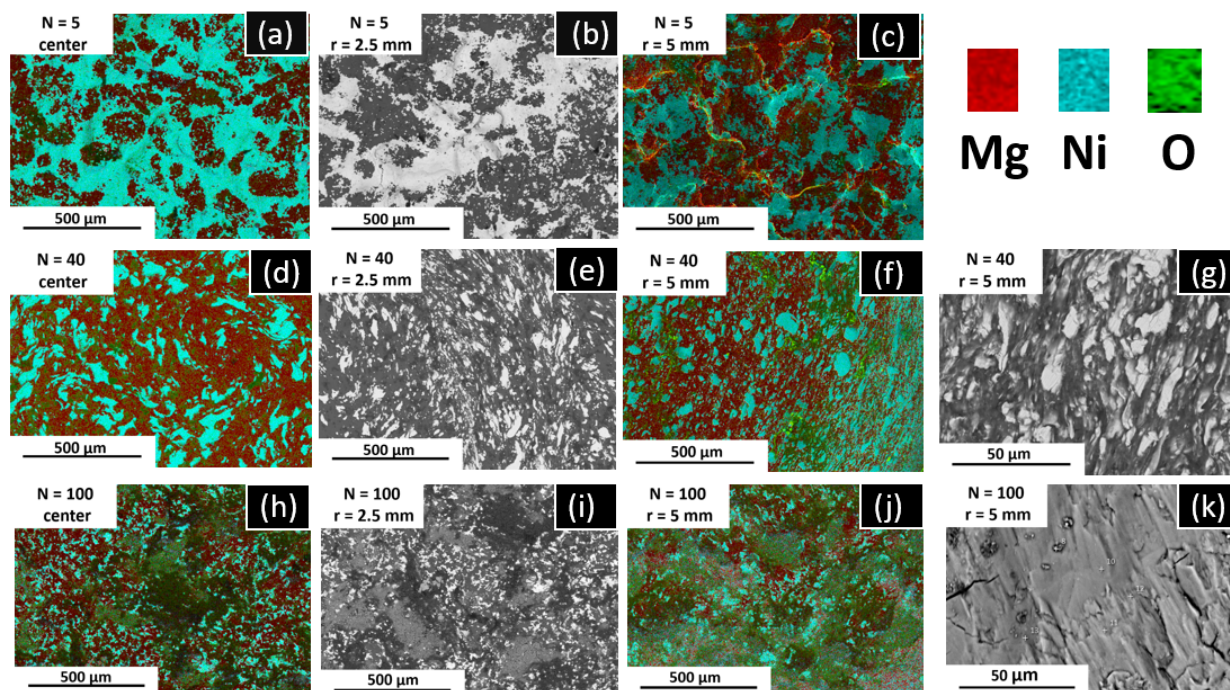
Figure 4. SEM BSE micrographs (**b**,**e**,**g**,**i**,**k**) and EDS elemental mapping analysis (**a**,**c**,**d**,**f**,**h**,**j**) of Mg powder (**a**) and Mg-30 at% Ni after HPT processing for different numbers of turns, taken from center (left, (**a**,**d**,**f**)), the middle (**b**,**e**,**i**), and the edge of the disc (**c**,**f**,**g**,**j**,**k**). Bright and dark contrast in SEM micrographs correspond to Ni and Mg, respectively.
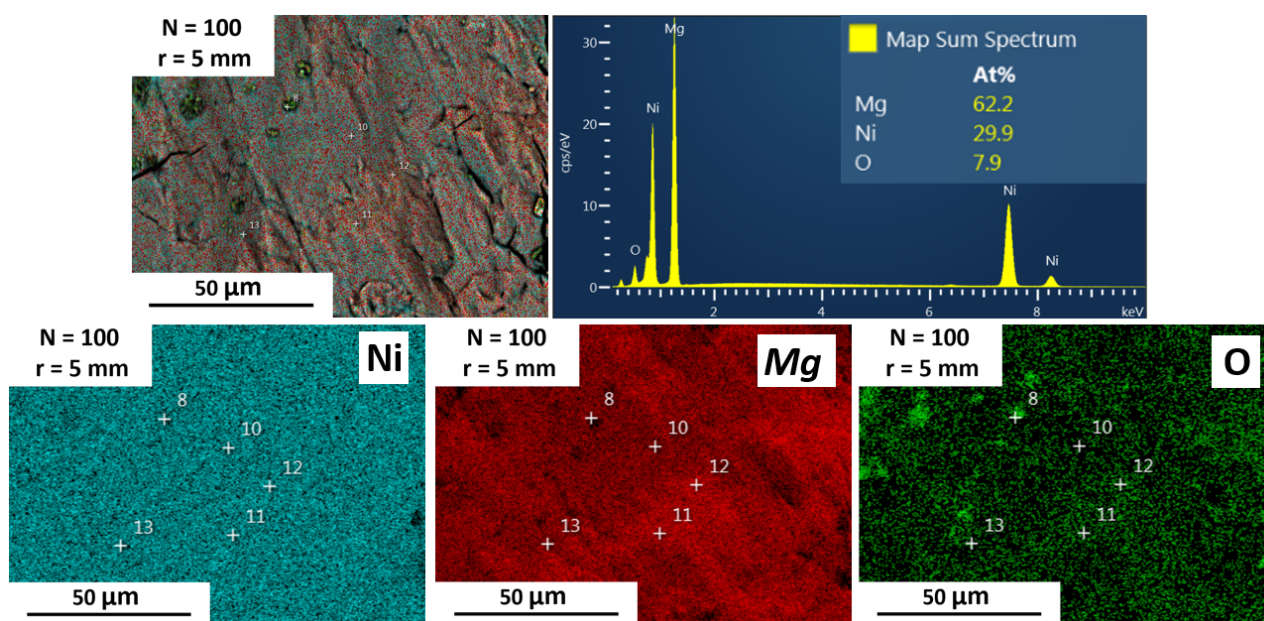

Figure 5. EDS mapping analysis of Mg-30 at% Ni processed for 100 turns at the edge of the disc (r = 5 mm, γ = 4400). The + sign indicated the spots where EDS compositions where recorded.

3.2. Hydrogen Storage Properties of Mg-Ni Processed by HPT

Figure 6 shows the hydrogenation kinetics of Mg-30 at% Ni processed with 3, 10, 20, 50, and 100 turns. It should be noted that the hydrogenation tests were performed several weeks after the HPT processing and that the samples were left in the air during the whole period. Therefore, these tests also indicate the air resistance of the HPT-processed samples. Samples with 20 and 100 turns show a maximum capacity of 3.8 wt% of hydrogen at 350 °C

after 18 h, which is close to the nominal capacity of the material (3.9 wt%). Samples with 3 and 50 turns show a lower capacity of 3.7 wt% after 20 h, while the storage capacity of the sample with heat treatment is reduced to 3.4 wt% after 24 h. According to this, the sample N100 optimizes both the synthesizing and storage capacity. The hydrogen storage capacity obtained in this work is higher than the capacity reported for Mg-Ni processed by different severe plastic deformation processes, as shown in Table 4, such as high-energy ball milling (HEBM) (2.4 wt%), HEBM + HPT (3 wt%), casting + HPT (3.3 wt%), HEBM with cold rolling (2.4 wt%), and HEBM + ECAP (1.5 wt%) [44,58,73,74]. Figure 6 also shows the activation results of a commercially pure (CP) Mg process with three turns for comparison purposes. It is clear in Figure 6 that the addition of Ni helps to accelerate the absorption of Mg even just after three turns of HPT.
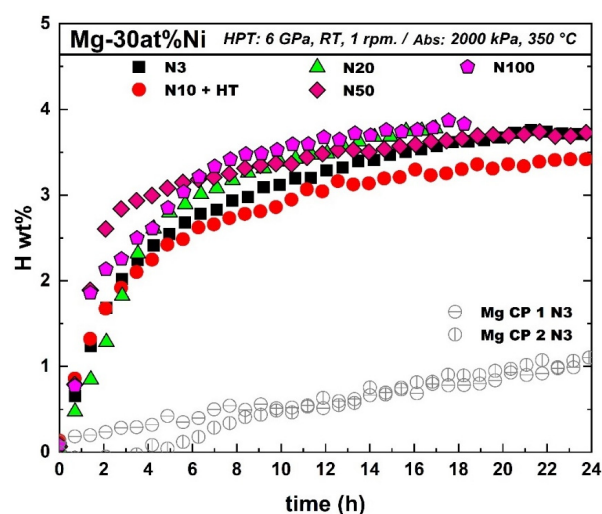

Figure 6. Hydrogenation results of commercially pure Mg after 3 turns and Mg-30 at% Ni after 3, 10, 20, 50, and 100 turns of HPT.

Table 4. Hydrogen storage of some Mg-Ni systems processed by SPD process.

Sample + Condition	Synthesis Process	SPD Process	Activation	Ref.
Mg_2Ni/annealing	Casting	-	2.2 wt%, 20 h	
Mg_2Ni/annealing + HPT	Casting	HPT, 6 GPa, N10	3.3 wt%, 20 h	[58]
Mg_2Ni/annealing + HPT + annealing	Casting	HPT, 6 GPa, N10	3.3 wt%, 20 h	
Mg-25 at% Ni/HEBM+ HPT	HEBM	HPT, 2 GPa, N5	1.6 wt%, 5 h	[73]
Mg-25 at% Ni/HEBM+ CR4	HEBM 10h	Cold rolling	2.4 wt%, 0.5 h	
Mg-25 at% Ni/HEBM+ CR10	HEBM 10h	Cold rolling	2.4 wt%, 1 h	
Mg-25 at% Ni/HEBM+ ECAP 2x	HEBM 10h	ECAP	1.5 wt%, 0.5 h	[44]
Mg-25 at% Ni/HEBM+ ECAP 6x	HEBM 10h	ECAP	1.5 wt%, 0.5 h	
Mg-30 at% Ni/HEBM	HEBM 1h	-	2 wt%, 0.5 h	
Mg-30 at% Ni/HEBM + HPT	HEBM 1h	HPT, 6 GPa, N5	3 wt%, 1.7 h	
Mg-30 at% Ni/HEBM	HEBM 10h	-	2.4 wt, 0.5 h	[74]
Mg-30 at% Ni/HEBM + HPT	HEBM 10h	HPT, 6 GPa, N5	3 wt%, 1.7 h	
Mg-30 at% Ni/HPT (+60 days in Air)	HPT: 6 GPa, 1 rpm, N= 3–100		3.8 wt%, 18 h	This work

In order to evaluate the hydride formation in the Mg-Ni system, XRD patterns were taken after the hydrogen absorption test. Figure 7 shows the diffraction pattern for the activated Mg-30 at% Ni with 50 and 100 HPT turns. The XRD results confirm the formation of hydride phases after the hydrogenation test for all the samples. Further analysis by Rietveld refinement confirms the formation of MgH_2 and Mg_2NiH_4 in Mg-30 at% Ni after 100 turns, as shown in Figure 7.
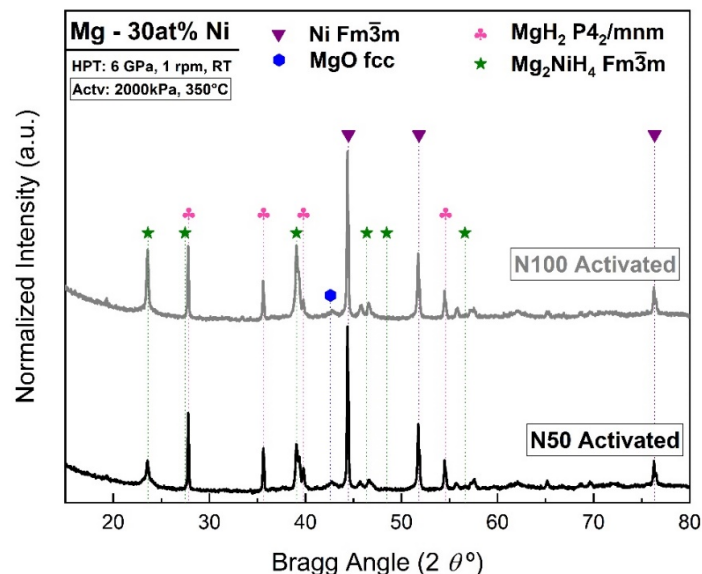
Figure 7. XRD patterns showing hydride formation in Mg-30 at% Ni processed by HPT for 50 and 100 turns and activated under 2000 kPa and 350 °C.

Table 5 summarizes the Rietveld refinement results for Mg-30 at% Ni processed by HPT for 50 and 100 turns after first hydrogenation (activation). It can be seen that when increasing from 50 to 100 turns, the amount of Mg_2Ni hydride phase also increases, which means a reduction in the amount of MgH_2 and Ni phases. A MgO phase has also been identified after the activation test; this oxide phase was not identified in the powder mixture before HPT processing by XRD, as shown in Figure 1 and Table 1, which suggests that the oxide phase increases during the manipulation after the activation test, probably due to fresh surface exposed.

Table 5. Crystallographic parameters of the phases present after first hydrogenation (activation) of Mg-30 at% Ni processed by HPT.

Condition	Phase	wt%	a (Å)	c (Å)	Crystallite Size (nm)
HPT	Ni fcc	25 (1)	3.5252 (1)	-	103 (4)
N50, $\gamma = 2000$	MgH2	23 (1)	4.5181 (3)	3.0224 (3)	127 (18)
Activated	MgO	22 (2)	4.218 (3)	-	5 (1)
	Mg_2NiH_4	31 (1)	14.614 (4)	b = 6.415 (2), c= 6.494 (3), beta = 115.7 (1)	24 (1)
HPT	Ni fcc	22.5 (9)	3.5251 (14)	-	91 (3)
N100, $\gamma = 4400$	MgH_2	17.0 (8)	4.5184 (3)	3.0225 (3)	162 (12)
Activated	MgO	23 (2)	4.216 (4)	-	3.2 (3)
	Mg_2NiH_4	38 (2)	14.6163 (18)	b = 6.426 (4), c = 6.489 (1), beta = 115.9° (1)	40 (1)

4. Conclusions

Mechanical synthesis of Mg_2Ni has been achieved for the first time through HPT processing directly from binary elemental powder mixtures. This study shows that through HPT processing, it is possible to synthesize the intermetallic compound from the powder mixture via a solid-state reaction. The result is in good agreement with previous research where new phase formations of $Mg_{17}Al_{12}$, MgZn, MgAg, MgIn, and Mg_2Sn were also synthesized by solid-stated reactions under 3 GPa and 100 turns of HPT [36].

It was also found that pressure is an important parameter that affects the phase transformation during HPT and hydrogen storage properties. The present results show

that at 6 GPa, it was possible to detect Mg_2Ni by XRD after 50 turns without any heat treatment, which was not reported in HPT performed under 3 GPa after 100 turns [36]. The present results confirm a maximum amount of 59 wt% of Mg_2Ni phase after 100 turns of HPT. It was also possible to identify that phase formation increased along the axial and radial directions of the disc, following the strain increment. This suggests that HPT is a powerful method to synthesize intermetallic compounds that can be difficult to fabricate by conventional means.

Regarding the alloying synthesis process of Mg_2Ni, the sample with 100 turns showed the highest amount of Mg_2Ni and the highest storage capacity. Accordingly, it seems this is the optimum number of turns for the hydrogen storage capacity.

Finally, an interesting result of this research is that complete hydrogen absorption by the Mg-Ni system was observed after several weeks of air exposure for all Mg-30 at% Ni samples. This indicates that the HPT-processed samples have good air resistance.

Nomenclature

a	a lattice parameter in x,y,y (a,b,c) system	h	thickness of the disc
Abs	absorption	hcp	hexagonal compact structure
Activ	activation	HT	heat treatment
Å	Angström unit	HEBM	high-energy ball milling
at%	atomic percentage	$K\alpha$	k alpha radiation
bcc	body-cubic center structure	N	number of HPT turns
c	c lattice parameter in x,y,y (a,b,c) system	r	radius
CP	commercially pure	RT	room temperature
ECAP	equal-channel angular processing	wt%	weight percentage
fcc	face-center cubic structure	γ	equivalent shear strain

References

1. James, B.D. Overview of Hydrogen Storage Technologies. 2008, pp. 568–569. Available online: https://citeseerx.ist.psu.edu/document?repid=rep1&type=pdf&doi=2b733c606694f44cf0dcb744c94c3161d3aca4bb (accessed on 22 August 2024).
2. Paster, M.D.; Ahluwalia, R.K.; Berry, G.; Elgowainy, A.; Lasher, S.; McKenney, K.; Gardiner, M. Hydrogen Storage Technology Options for Fuel Cell Vehicles: Well-to-Wheel Costs, Energy Efficiencies, and Greenhouse Gas Emissions. *Int. J. Hydrogen Energy* **2011**, *36*, 14534–14551. [CrossRef]
3. Arjona, V.T.; Ast, C.; Thompson, S.; Fellow, O. Hydrogen and Fuel Cells Overview. Available online: https://www.energy.gov/eere/fuelcells/hydrogen-and-fuel-cell-technologies-office-information-resources (accessed on 14 July 2024).
4. Yamashita, A.; Kondo, M.; Goto, S.; Ogami, N. *Development of High-Pressure Hydrogen Storage System for the Toyota "Mirai."*; SAE Technical Paper 2015-01-1169; SAE International: Warrendale, PA, USA, 2015.
5. Latroche, M. Structural and Thermodynamic Properties of Metallic Hydrides Used for Energy Storage☆. *J. Phys. Chem. Solids* **2004**, *65*, 517–522. [CrossRef]
6. Rusman, N.A.A.; Dahari, M. A Review on the Current Progress of Metal Hydrides Material for Solid-State Hydrogen Storage Applications. *Int. J. Hydrogen Energy* **2016**, *41*, 12108–12126. [CrossRef]

7. Young, K. Metal Hydrides☆. In *Reference Module in Chemistry, Molecular Sciences and Chemical Engineering*; Elsevier: Amsterdam, The Netherlands, 2018.
8. Srinivasan, S.S.; Demirocak, D.E. Metal Hydrides Used for Hydrogen Storage. In *Nanostructured Materials for Next-Generation Energy Storage and Conversion: Hydrogen Production, Storage, and Utilization*; Springer: Berlin/Heidelberg, Germany, 2017; pp. 225–255. ISBN 9783662535141.
9. Dornhel, M. Thermodynamics of Metal Hydrides: Tailoring Reaction Enthalpies of Hydrogen Storage Materials. In *Thermodynamics—Interaction Studies—Solids, Liquids and Gases*; IntechOpen: London, UK, 2011; pp. 891–911.
10. Tanaka, T.; Ketta, M.; Azofeifa, D.E. Theory of Hydrogen Absorption in Metal Hydrides. *Phys. Rev. B* **1981**, *24*, 1771. [CrossRef]
11. Huot, J.; Edalati, K.; Stefano, D.; Yaroslav, F. Mechanochemistry of Metal Hydrides: Recent Advances. *Materials* **2019**, *12*, 2778. [CrossRef] [PubMed]
12. Grataetz, J.; Reilly, J.J.; Wegrzyn, J. Metal Hydrides for Hydrogen Storage. In *Materials Research Society Symposium—Proceedings*; Materials Research Society: Warrendale, PA, USA, 2008; Volume 1041.
13. Shelyapina, M.G. Metal Hydrides for Energy Storage. In *Handdbook of Evomaterials*; Martínez, L., Kharissova, O., Kharisov, B., Eds.; Springer International Publishing AG: Cham, Switzerland, 2018.
14. Liu, H.; Zhang, J.; Sun, P.; Zhou, C.; Liu, Y.; Fang, Z.Z. Effect of Oxygen on the Hydrogen Storage Properties of TiFe Alloys. *J. Energy Storage* **2022**, *55*, 105543. [CrossRef]
15. Liu, H.; Zhang, J.; Sun, P.; Zhou, C.; Liu, Y.; Fang, Z.Z. Effect of Oxygen Addition on Phase Composition and Activation Properties of TiFe Alloy. *Int. J. Hydrogen Energy* **2022**, *48*, 8563–8572. [CrossRef]
16. Yadav, D.K.; Chawla, K.; Pooja; Lal, N.; Choudhary, B.L.; Lal, C. Catalytic Effect of TiO2 on Hydrogen Storage Properties of MgH_2. *Mater. Today Proc.* **2021**, *46*, 2326–2329. [CrossRef]
17. Lobo, N.; Klimkowicz, A.; Takasaki, A. Effect of TiO_2 + Nb_2O_5 + TiH_2 Catalysts on Hydrogen Storage Properties of Magnesium Hydride. *MRS Adv.* **2020**, *5*, 1059–1069. [CrossRef]
18. Korablov, D.; Nielsen, T.K.; Bessencacher, F.; Jensen, T.R. Mechanism and Kinetics of Early Transition Metal Hydrides, Oxides, and Chlorides to Enhance Hydrogen Release and Uptake Properties of MgH_2. *Powder Diffr.* **2015**, *30*, S9–S15. [CrossRef]
19. Borgschulte, A.; Rector, J.H.; Dam, B.; Grissen, R.; Zuttel, A. The Role of Niobium Oxide as a Surface Catalyst for Hydrogen Absorption. *J. Catal.* **2005**, *235*, 353–358. [CrossRef]
20. Barkhordarian, G.; Rudiger Bormann, T.K. Fast Hydrogen Sorption Kinetics of Nanocrystalline Mg Using Nb_2O_5 as Catalyst. *Scr. Mater.* **2003**, *49*, 213–217. [CrossRef]
21. Oelerich, W.; Klassen, R.; Klassen, R. Comparison of the Catalytic Effects of V, V2O5, VN, and VC on the Hydrogen Sorption of Nanocrystalline Mg. *J. Alloys Compd.* **2001**, *322*, 5–9. [CrossRef]
22. Oelerich, W.; Klassen, R.; Bormann, R. Metal Oxides as Catalysts for Improved Hydrogen Sorption in Nanocrystalline Mg-Based Materials. *J. Alloys Compd.* **2000**, *315*, 237–242. [CrossRef]
23. Dematteis, E.M.; Berti, N.; Cuevas, F.; Latroche, M.; Baricco, M. Substitutional Effects in TiFe for Hydrogen Storage: A Comprehensive Review. *Mater. Adv.* **2021**, *2*, 2524–2560. [CrossRef]
24. Park, K.B.; Na, T.W.; Kim, Y.D.; Park, J.Y.; Kang, J.W.; Kang, H.S.; Park, K. Characterization of Microstructure and Surface Oxide of Ti1.2Fe Hydrogen Storage Alloy. *Int. J. Hydrogen Energy* **2021**, *46*, 13082–13087. [CrossRef]
25. Sun, D.; Enoki, H.; Gingl, F.; Akiba, E. *New Approach for Synthesizing Mg-Based Alloys*; Elsevier: Amsterdam, The Netherlands, 1999; Volume 285.
26. Janot, R.; Aymard, L.; Rougier, A.; Tarascon, J.M. Fast Hydrogen Sorption Kinetics for Ball-Milled Mg_2Ni Alloys. *J. Phys. Chem. Solids* **2004**, *65*, 529–534. [CrossRef]
27. Huot, J.; Liang, G.; Boily, S.; Van Neste, A.; Schulz, R. Structural Study and Hydrogen Sorption Kinetics of Ball-Milled Magnesium Hydride. *J. Alloys Compd.* **1999**, *295*, 495–500. [CrossRef]
28. Sapassov, T.; Solsana, P.; Suriñach, S.; Baró, M.D. Optimisation of the Ball-Milling and Heat Treatment Parameters for Syntesis of Amorphous and Nanocrystalline Mg2Ni-Based Alloys. *J. Alloys Compd.* **2003**, *349*, 242–254. [CrossRef]
29. Lototskyy, M.; Sibanyoni, J.M.; Denys, R.V.; Williams, M.; Pollet, B.G.; Yartys, V.A. Magnesium—Carbon Hydrogen Storage Hybrid Materials Produced by Reactive Ball Milling in Hydrogen Magnesium—Carbon Hydrogen Storage Hybrid Materials Produced by Reactive Ball Milling in Hydrogen. *Carbon* **2013**, *57*, 146–160. [CrossRef]
30. Wu, Y.; Han, W.; Zhou, S.X.; Lototsky, M.V.; Solberg, J.K.; Yartys, V.A. Microstructure and Hydrogenation Behavior of Ball-Milled and Melt-Spun Mg—10Ni–2Mm Alloys. *J. Alloys Compd.* **2008**, *466*, 176–181. [CrossRef]
31. Kurnia-Dewa, M.D.; Wiryolukito, S.; Suwarno, H. Hydrogen Absorption Capacity of Fe-Ti-Al Alloy Prepared by High Energy Ball Milling. *Energy Procedia* **2015**, *68*, 316–325. [CrossRef]
32. Iturbe-García, J.L.; García-Núñez, M.R.; López-Muñoz, B.E. Synthesis of the Mg2Ni Alloy Prepared by Mechanical Alloying Using a High Energy Ball Mill. *J. Mex. Chem. Soc.* **2010**, *54*, 46–50. [CrossRef]
33. Phasha, M.; Maweja, K.; Babst, C. Mechanical Alloying by Ball Milling of Ti and Mg Elemental Powders: Operation Condition Considerations. *J. Alloys Compd.* **2010**, *492*, 201–207. [CrossRef]
34. Leiva, D.R.; De Almeida Costa, H.C.; Huot, J.; Santos Pinhero, T.; Jorge, M., Jr.; Tomishimi Ishikawa, T.; Botta, W.J. Magnesium-Nickel Alloy for Hydrogen Storage Produced by Melt Spinning Followed by Cold Rolling. *Mater. Res.* **2012**, *15*, 813–817. [CrossRef]

35. Kudriashova, N.; Huot, J. Effect of Cold Rolling on Magnesium-Based Metal Hydrides. *Mater. Trans.* **2023**, *64*, 1879–1885. [CrossRef]

36. Emami, H.; Edalati, K.; Staykov, A.; Hongo, T.; Iwaoka, H.; Horita, Z.; Akiba, E. Solid-State Reactions and Hydrogen Storage in Magnesium Mixed with Various Elements by High-Pressure Torsion: Experiments and First-Principles Calculations. *RSC Adv.* **2016**, *6*, 11665–11674. [CrossRef]

37. López Gómez, E.I.; Edalati, K.; Antiqueira, F.J.; Coimbrão, D.D.; Zepon, G.; Leiva, D.R.; Ishikawa, T.T.; Cubero-Sesin, J.M.; Botta, W.J. Synthesis of Nanostructured TiFe Hydrogen Storage Material by Mechanical Alloying via High-Pressure Torsion. *Adv. Eng. Mater.* **2020**, *22*, 2000011. [CrossRef]

38. Edalati, K.; Emami, H.; Ikeda, Y.; Iwaoka, H.; Tanaka, I.; Akiba, E.; Horita, Z. New Nanostructured Phases with Reversible Hydrogen Storage Capability in Immiscible Magnesium-Zirconium System Produced by High-Pressure Torsion. *Acta Mater.* **2016**, *108*, 293–303. [CrossRef]

39. Edalati, K.; Emami, H.; Staykov, A.; Smith, D.J.; Akiba, E.; Horita, Z. Formation of Metastable Phases in Magnesium-Titanium System by High-Pressure Torsion and Their Hydrogen Storage Performance. *Acta Mater.* **2015**, *99*, 150–156. [CrossRef]

40. López-Gómez, E.I.; Edalati, K.; Coimbrão, D.D.; Antiqueira, F.J.; Zepon, G.; Cubero-Sesin, J.M.; Botta, W.J. FCC Phase Formation in Immiscible Mg-Hf (Magnesium-Hafnium) System by High-Pressure Torsion. *AIP Adv.* **2020**, *10*, 055222. [CrossRef]

41. Edalati, K. Metallurgical Alchemy by Ultra-Severe Plastic Deformation via High-Pressure Torsion Process. *Mater. Trans.* **2019**, *60*, 1221–1229. [CrossRef]

42. Edalati, K.; Horita, Z. A Review on High-Pressure Torsion (HPT) from 1935 to 1988. *Mater. Sci. Eng. A* **2016**, *652*, 325–352. [CrossRef]

43. Oh-ishi, K.; Edalati, K.; Kim, H.S.; Hono, K.; Horita, Z. High-Pressure Torsion for Enhanced Atomic Diffusion and Promoting Solid-State Reactions in the Aluminum–Copper System. *Acta Mater.* **2013**, *61*, 3482–3489. [CrossRef]

44. Révész, Á.; Gajdics, M.; Varga, L.K.; Krállics, G.; Péter, L. Hydrogen Storage of Nanocrystalline Mg-Ni Alloy Processed by Equal-Channel Angular Pressing and Cold Rolling. *Int. J. Hydrogen Energy* **2014**, *39*, 9911–9917. [CrossRef]

45. Wang, L.; Jiang, J.; Ma, A.; Li, Y.; Song, D. A Critical Review of Mg-Based Hydrogen Storage Materials Processed by Equal Channel Angular Pressing. *Metals* **2017**, *7*, 324. [CrossRef]

46. Krystian, M.; Zehetbauer, M.J.; Kropik, H.; Mingler, B.; Krexner, G. Hydrogen Storage Properties of Bulk Nanostructured ZK60 Mg Alloy Processed by Equal Channel Angular Pressing. *J. Alloys Compd.* **2011**, *5095*, 5449–5455. [CrossRef]

47. Skripnyuk, V.M.; Rabkin, E.; Estrin, Y.; Lapovok, R. Improving Hydrogen Storage Properties of Magnesium Based Alloys by Equal Channel Angular Pressing. *Int. J. Hydrogen Energy* **2009**, *34*, 6320–6324. [CrossRef]

48. Asselli, A.A.C.; Leiva, D.R.; Huot, J.; Kawasaki, M.; Langdon, T.G.; Botta, W.J. Effects of Equal-Channel Angular Pressing and Accumulative Roll-Bonding on Hydrogen Storage Properties of a Commercial ZK60 Magnesium Alloy. *Int. J. Hydrogen Energy* **2015**, *40*, 16971–16976. [CrossRef]

49. Edalati, K.; Matsuda, J.; Yanagida, A.; Akiba, E.; Horita, Z. Activation of TiFe for Hydrogen Storage by Plastic Deformation Using Groove Rolling and High-Pressure Torsion: Similarities and Differences. *Int. J. Hydrogen Energy* **2014**, *39*, 15589–15594. [CrossRef]

50. Edalati, K.; Matsuda, J.; Iwaoka, H.; Toh, S.; Akiba, E.; Horita, Z. High-Pressure Torsion of TiFe Intermetallics for Activation of Hydrogen Storage at Room Temperature with Heterogeneous Nanostructure. *Int. J. Hydrogen Energy* **2013**, *38*, 4622–4627. [CrossRef]

51. Edalati, K.; Shao, H.; Emami, H.; Iwaoka, H.; Akiba, E.; Horita, Z. Activation of Titanium-Vanadium Alloy for Hydrogen Storage by Introduction of Nanograins and Edge Dislocations Using High-Pressure Torsion. *Int. J. Hydrogen Energy* **2016**, *41*, 8917–8924. [CrossRef]

52. Edalati, K.; Akiba, E.; Horita, Z. High-Pressure Torsion for New Hydrogen Storage Materials. *Sci. Technol. Adv. Mater.* **2018**, *19*, 185–193. [CrossRef]

53. Edalati, K.; Yamamoto, A.; Horita, Z.; Ishihara, T. High Pressure Torsion of Pure Magnesium: Evolution of Mechanical Properties, Microstructure and Hydrogen Storage Capacity with Equivalent Strain. *Scr. Mater.* **2011**, *64*, 880–883. [CrossRef]

54. Kitabayashi, K.; Edalati, K.; Li, H.-W.; Akiba, E.; Horita, Z. Phase Transformations in MgH$_2$–TiH$_2$ Hydrogen Storage System by High-Pressure Torsion Process. *Adv. Eng. Mater.* **2018**, *22*, 1900027. [CrossRef]

55. He, L.; Shi, X.; Li, X.; Huang, J.; Cheng, T.; Wang, X.; Li, Y.; Lin, H.; Edalati, K.; Li, H.-W. Severe Plastic Deformation through High-Pressure Torsion for Preparation of Hydrogen Storage Materials—A Review. *Mater. Trans.* **2023**, *64*, 1575–1584. [CrossRef]

56. Révész, Á.; Gajdics, M. The Effect of Severe Plastic Deformation on the Hydrogen Storage Properties of Metal Hydrides. *Mater. Trans.* **2023**, *64*, 1387–1400. [CrossRef]

57. Edalati, K.; Ahmed, A.Q.; Akrami, S.; Ameyama, K.; Aptukov, V.; Asfandiyarov, R.N.; Ashida, M.; Astanin, V.; Bachmaier, A.; Beloshenko, V.; et al. Severe Plastic Deformation for Producing Superfunctional Ultrafine-Grained and Heterostructured Materials: An Interdisciplinary Review. *J. Alloys Compd.* **2024**, *1002*, 174667. [CrossRef]

58. Hongo, T.; Edalati, K.; Arita, M.; Matsuda, J.; Akiba, E.; Horita, Z. Significance of Grain Boundaries and Stacking Faults on Hydrogen Storage Properties of Mg$_2$Ni Intermetallics Processed by High-Pressure Torsion. *Acta Mater.* **2015**, *92*, 46–54. [CrossRef]

59. Edalati, K.; Uehiro, R.; Ikeda, Y.; Li, H.-W.; Emami, H.; Filinchuk, Y.; Arita, M.; Sauvage, X.; Tanaka, I.; Akiba, E.; et al. Design and Synthesis of a Magnesium Alloy for Room Temperature Hydrogen Storage. *Acta Mater.* **2018**, *149*, 88–96. [CrossRef]

60. Liu, X.; Zhu, Y.; Li, L. Structure and Hydrogenation Properties of Nanocrystalline Mg$_2$Ni Prepared by Hydriding Combustion Synthesis and Mechanical Milling. *J. Alloys Compd.* **2008**, *455*, 197–202. [CrossRef]

61. Suryanarayana, C. Mechanical Alloying and Milling. *Prog. Mater. Sci.* **2001**, *46*, 1–184. [CrossRef]
62. Liu, Y.; Chabane, D.; Elkedim, O. Intermetallic Compounds Synthesized by Mechanical Alloying for Solid-State Hydrogen Storage: A Review. *Energies* **2021**, *14*, 5758. [CrossRef]
63. Ruslan, Z.; Valiev, R.; Estrin, Y.; Horita, Z.; Langdon, T.G.; Zehetbauer, M.J.; Zhu, Y.T. Producing Bulk Ultrafine-Grained Meterials by Severe Plastic Deformation. *JOM* **2006**, *58*, 33–39. [CrossRef]
64. Faddegon, B.; Ramos-Méndez, J.; Schuemann, J.; McNamara, A.; Shin, J.; Perl, J.; Paganetti, H. The TOPAS Tool for Particle Simulation, a Monte Carlo Simulation Tool for Physics, Biology and Clinical Research. *Phys. Med.* **2020**, *72*, 114–121. [CrossRef]
65. Perl, J.; Shin, J.; Schümann, J.; Faddegon, B.; Paganetti, H. TOPAS: An Innovative Proton Monte Carlo Platform for Research and Clinical Applications. *Med. Phys.* **2012**, *39*, 6818–6837. [CrossRef]
66. Gunderov, D.V.; Asfandiyarov, R.N.; Astanin, V.V.; Sharafutdinov, A.V. Slippage during High-Pressure Torsion: Accumulative High-Pressure Torsion—Overview of the Latest Results. *Metals* **2023**, *13*, 1340. [CrossRef]
67. Edalati, K.; Uehiro, R.; Fujiwara, K.; Ikeda, Y.; Li, H.-W.; Sauvage, X.; Valiev, R.Z.; Akiba, E.; Tanaka, I.; Horita, Z. Ultra-Severe Plastic Deformation: Evolution of Microstructure, Phase Transformation and Hardness in Immiscible Magnesium-Based Systems. *Mater. Sci. Eng. A* **2017**, *701*, 158–166. [CrossRef]
68. Castro, M.M.; Sabbaghianrad, S.; Pereira, P.H.R.; Mazzer, E.M.; Isaac, A.; Langdon, T.G.; Figueiredo, R.B. A Magnesium-Aluminium Composite Produced by High-Pressure Torsion. *J. Alloys Compd.* **2019**, *804*, 421–426. [CrossRef]
69. Cubero-Sesin, J.M.; Horita, Z. Powder Consolidation of Al-10wt% Fe Alloy by High-Pressure Torsion. *Mater. Sci. Eng. A* **2012**, *558*, 462–471. [CrossRef]
70. Ibrahim, N.; Peterlechner, M.; Emeis, F.; Wegner, M.; Divinski, S.V.; Wilde, G. Mechanical Alloying via High-Pressure Torsion of the Immiscible Cu50Ta50 System. *Mater. Sci. Eng. A* **2017**, *685*, 19–30. [CrossRef]
71. Edalati, K.; Daio, T.; Lee, S.; Horita, Z.; Nishizaki, T.; Akune, T.; Nojima, T.; Sasaki, T. High Strength and Superconductivity in Nanostructured Niobium-Titanium Alloy by High-Pressure Torsion and Annealing: Significance of Elemental Decomposition and Supersaturation. *Acta Mater.* **2014**, *80*, 149–158. [CrossRef]
72. Campos-Quirós, A.; Cubero-Sesín, J.M.; Edalati, K. Synthesis of Nanostructured Biomaterials by High-Pressure Torsion: Effect of Niobium Content on Microstructure and Mechanical Properties of Ti-Nb Alloys. *Mater. Sci. Eng. A* **2020**, *795*, 139972. [CrossRef]
73. Gajdics, M.; Calizzi, M.; Pasquini, L.; Schafler, E.; Révész, Á. Characterization of a Nanocrystalline Mg–Ni Alloy Processed by High-Pressure Torsion during Hydrogenation and Dehydrogenation. *Int. J. Hydrogen Energy* **2016**, *41*, 9803–9809. [CrossRef]
74. Révész, A.; Kánya, Z.; Verebélyi, T.; Szabó, P.J.; Zhilyaev, A.P.; Spassov, T. The Effect of High-Pressure Torsion on the Microstructure and Hydrogen Absorption Kinetics of Ball-Milled $Mg_{70}Ni_{30}$. *J. Alloys Compd.* **2010**, *504*, 83–88. [CrossRef]